Bulk and Surface Reactivity of $LiNi_{0.5}Mn_{1.5}O_4$ in Contact with (Acidic) Water

Annika R. Schuer, Matthias Kuenzel, Maider Zarrabeitia, Tobias Eisenmann, Chengping Li, Sylvio Indris, Michael Knapp, Volodymyr Baran, Ralph Gilles, Dorin Geiger, Ute Kaiser, Philipp Scheitenberger, Mika Lindén, Peter Axmann, Margret Wohlfahrt-Mehrens, Stefano Passerini,* and Dominic Bresser*

Lithium-ion battery cathode materials such as $LiNi_{0.5}Mn_{1.5}O_4$ (LNMO) are very sensitive to water, which has so far hindered the successful commercialization of aqueous electrode processing strategies. Herein, a detailed investigation of the surface and bulk reactivity of ordered LNMO with water and an aqueous solution of phosphoric acid to decipher the reaction mechanism and the impact on the eventual electrochemical behavior is presented. The comprehensive analysis via, for instance, neutron diffraction and synchrotron X-Ray diffraction, X-Ray absorption spectroscopy, magic-angle spinning nuclear magnetic resonance spectroscopy, thermogravimetric analysis coupled with mass spectrometry, high-resolution transmission electron microscopy, and X-Ray photoelectron spectroscopy reveals that the (acidic) water treatment particularly affects a very thin layer at the particle surface, while the bulk material remains largely unaffected. Nonetheless, when processed classically with *N*-methyl-2-pyrrolidone and polyvinylidene fluoride into electrodes, the significant impact of this layer on the electrochemical behavior highlights the important impact of the material surface on the eventually achievable performance in battery cells.

1. Introduction

As the lithium-ion battery market is growing continuously,[1,2] efforts to improve their sustainability are also increasing. On the one hand, this involves more sustainable materials, i.e., cobalt-free positive electrode active materials. On the other hand, more sustainable electrode fabrication processes, which eliminate harmful *N*-methyl-2-pyrrolidone (NMP) as a solvent and fluorinated polymeric binders, are also under investigation.[3–6] Currently, $LiCoO_2$ (LCO), $LiNi_{1-x-y}Co_xAl_yO_2$ (NCA), and $LiNi_{1-x-y}Mn_xCo_yO_2$ (NMC) are among the most widely used positive electrode materials; all containing cobalt as a key component. However, Co-free positive electrode materials exist, among which $LiNi_{0.5}Mn_{1.5}O_4$ (LNMO) is one of the most promising.[7] LNMO is de-/lithiated at potentials higher than 4.7 V versus Li^+/Li. Thus, it provides a comparable energy density as the above-mentioned cobalt-containing LCO, NCA, and NMC at the full-cell

A. R. Schuer, M. Kuenzel, M. Zarrabeitia, T. Eisenmann, S. Passerini, D. Bresser
Helmholtz Institute Ulm (HIU)
89081 Ulm, Germany
E-mail: stefano.passerini@kit.edu; dominic.bresser@kit.edu

A. R. Schuer, M. Kuenzel, M. Zarrabeitia, T. Eisenmann, S. Passerini, D. Bresser
Karlsruhe Institute of Technology (KIT)
76021 Karlsruhe, Germany

C. Li, S. Indris, M. Knapp
Institute for Applied Materials (IAM)
KIT
76344 Eggenstein-Leopoldshafen, Germany

The ORCID identification number(s) for the author(s) of this article can be found under https://doi.org/10.1002/aesr.202500101.

C. Li
Faculty of Materials Science and Engineering
Kunming University of Science and Technology
Kunming 650093, P. R. China

S. Indris
Applied Chemistry and Engineering Research Centre of Excellence (ACER CoE)
Université Mohammed VI Polytechnique (UM6P)
Lot 660, Hay Moulay Rachid, Ben Guerir 43150, Morocco

V. Baran, R. Gilles
Heinz Maier-Leibnitz Zentrum (MLZ)
Technische Universität München (TUM)
85748 Garching, Germany

V. Baran
Deutsches Elektronen-Synchrotron (DESY)
22607 Hamburg, Germany

D. Geiger, U. Kaiser
Electron Microscopy Group of Materials Science
Ulm University (UUlm)
89081 Ulm, Germany

level, despite its slightly lower theoretical specific capacity (147 mAh g^{-1}).[7–9] Independent from the choice of the lithium transition metal oxide, though, the state-of-the-art positive electrode production employs polyvinylidene difluoride (PVdF) as the binder and NMP as the solvent. Both are environmentally harmful, and the latter requires a rather complicated recycling process owing to its toxicity, and needs a high drying temperature, both resulting in rather high costs.[10]

Producing electrodes using water as the processing solvent could alleviate these issues and at the same time would be more environmentally friendly.[11,12] However, it has been found that lithium transition metal (TM) oxides, including LNMO, are sensitive toward water.[11,13–15] Contact with water is assumed to cause a Li$^+$/H$^+$ cation exchange, as already observed for disordered LNMO and similar materials, i.e., Li$_2$MnO$_3$ and LiMn$_2$O$_4$,[16–18] and recent studies have shown that this effect is even more pronounced for partially delithiated LNMO.[19] This leads to the loss of lithium, especially at the particle surface, resulting in poorer performance as well as reduced cycle life due to the structural changes originating from the surface reaction as reported, for example, for Ni-rich cathode materials or lithium iron phosphates.[14,15,20] Among the surface reactions, the formation of LiOH and TM hydroxides increases the pH of the electrode slurry, which attacks the Al$_2$O$_3$ passivation layer upon coating on the aluminum current collector.[21,22] This results in the delamination of the electrode and therefore the loss of contact between the active material and the current collector.[23] Loeffler et al.[21,24] showed that this effect can be mitigated by adding an acid to the slurry to reduce its pH, specifically phosphoric acid, as later confirmed by Kuenzel et al.[22] –an approach that has been well adopted also by other groups.[25–27] However, the instantly formed LiOH may still react with carbon dioxide from the air to form carbonates on the active material surface.[28] When the electrode is assembled into the cell, the Li$_2$CO$_3$ leads to side reactions with the organic electrolyte, causing CO$_2$/O$_2$ outgassing, especially in the first cycle,[29] and eventually leading to bloating of the cell, loss of contact and shortened cycle life. Studies on the long-term storage of NMC$_{811}$ under ambient atmosphere have revealed that not only Li$_2$CO$_3$ surface species are formed, in fact, but that the main surface species are nickel oxide hydroxides.[30,31]

Herein, we investigate the impact of short-term acidic and/or aqueous treatment of LNMO on its surface and bulk structure and chemistry by subjecting the material to a ball mill treatment comparable to the slurry preparation. The subsequent comprehensive and extensive structural investigation reveals that the impact of such treatments is largely limited to the outermost surface layer of the LNMO particles, though, having a significant effect on the eventual electrochemical behavior.

2. Results and Discussion

2.1. pH Evolution and Surface Characterization

As shown in **Figure 1**, the contact of LNMO with water, even for only very short times, has a significant impact on the pH of the aqueous suspension, resulting in a jump-like increase to 10 and more, that is, well beyond the aluminum passivation regime. To investigate the impact of the contact with water and, in comparison, with phosphoric acid to unveil the potential degradation mechanisms, the LNMO powder was exposed to an aqueous treatment (LNMO-H$_2$O) or a phosphoric acid treatment (LNMO-PA) simulating the aqueous slurry preparation. For this purpose, the LNMO powder was mixed in a 1:2 weight ratio with either DI water or an aqueous solution (0.5 wt%) of phosphoric acid and subjected to ball milling.

The recovered powdery samples were collected and studied first in detail by high-resolution transmission electron microscopy (HRTEM). The resulting TEM micrographs of the pristine and the treated samples are shown in **Figure 2**. For all samples, a well-crystallized structure is observed in the bulk of the particles. On the treated samples, however, a thin amorphous surface layer of ≈3–5 nm thickness is observed. To identify the surface chemical composition of this layer, X-ray photoelectron spectroscopy (XPS) measurements were carried out. From the XPS C 1s and O 1s core level regions (**Figure 3**a,b), it can be observed that on the pristine sample (LNMO-REF), besides adventitious carbon and ether group (intense purple peak at 285 eV and smaller green peak at 286.6 eV, respectively),[32,33] only very small quantities of Li$_2$CO$_3$ (289.6 eV)[33,34] and transition metal carbonates (TMCO$_3$, 288 eV)[32] are present. This is confirmed by the O 1s spectrum, where the M-O peak (530 eV)[35,36] is by far the most intense one, while only smaller amounts of carbonates (531.2 eV) and hydroxides (530.3 eV) are observed.
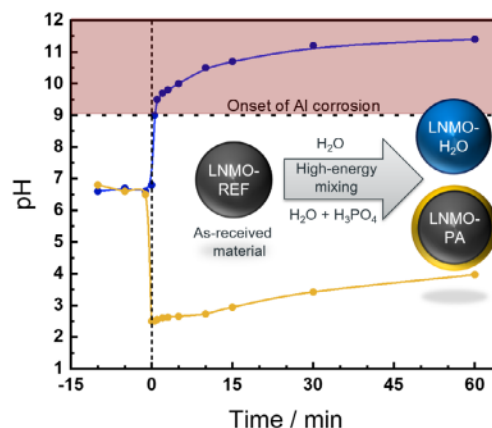
P. Scheitenberger, M. Lindén
Institute for Inorganic Chemistry II
Ulm University (UUlm)
89081 Ulm, Germany

P. Axmann, M. Wohlfahrt-Mehrens
Centre for Solar Energy and Hydrogen Research Baden-Württemberg (ZSW)
89081 Ulm, Germany

D. Bresser
Ulm University (UUlm)
89069 Ulm, Germany

Figure 1. Evolution of the pH over time when stirring LNMO powder in DI-water (blue point-line) or in an aqueous phosphoric acid (0.5 wt%) solution (yellow point-line). The vertical dashed line at $t = 0$ marks the addition of the LNMO powder (together with PA in the case of LNMO-PA).
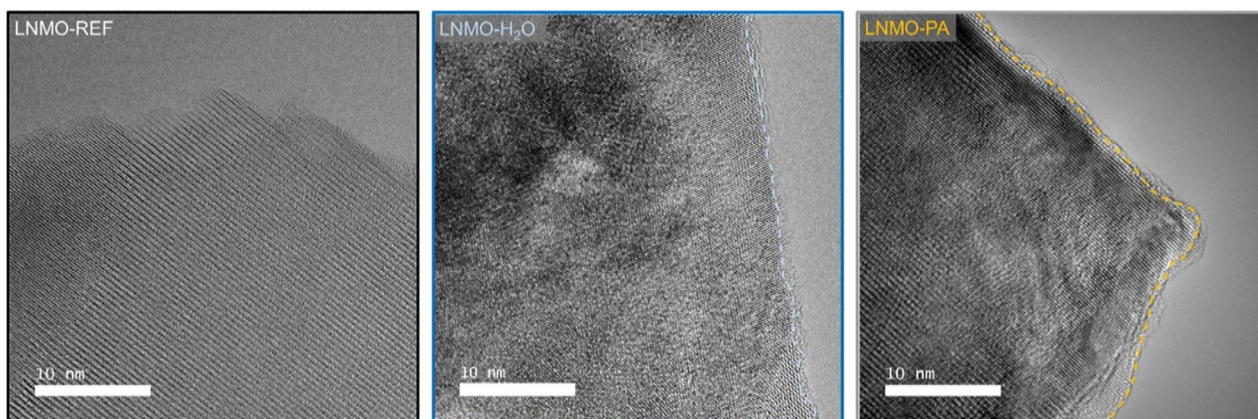
Figure 2. High-resolution TEM micrographs of pristine LNMO (LNMO-REF), LNMO-H_2O, and LNMO-PA. LNMO-H_2O and LNMO-PA show a thin amorphous layer of ≈3–5 nm thickness (dashed lines for the guidance of the eye).
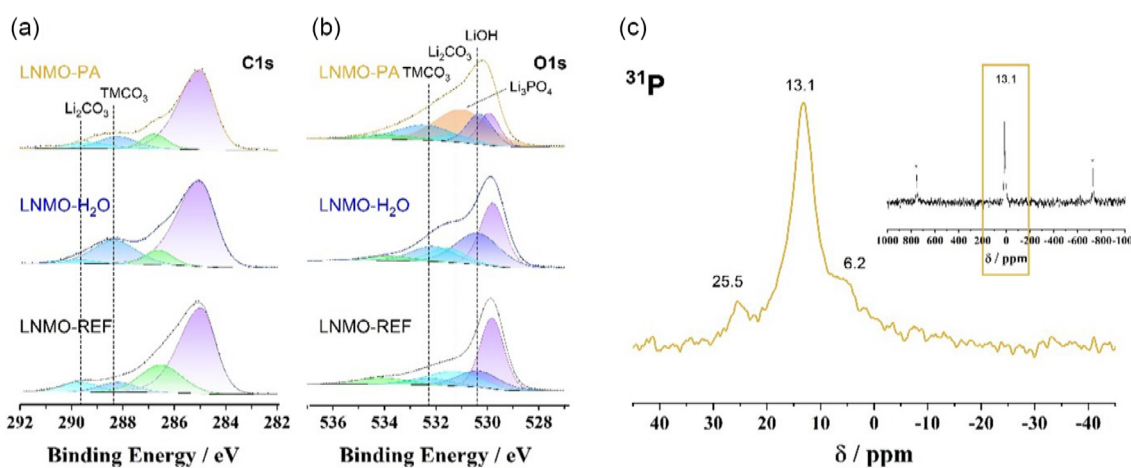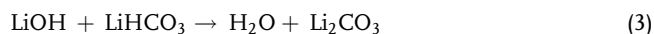

Figure 3. XPS core level of the a) C 1s and b) O 1s regions of LNMO-REF, LNMO-H_2O, and LNMO-PA. c) ^{31}P MAS NMR spectrum of LNMO-PA.

As a matter of fact, this is in very good agreement with the mechanism suggested by Shkrob et al.[37] involving the formation of LiOH upon contact with humidity, which is later converted into Li_2CO_3 by reaction with CO_2 from the air:

$$Li^+ + H_2O \rightarrow H^+ + LiOH \tag{1}$$

$$LiOH + CO_2 \rightarrow LiHCO_3 \tag{2}$$

$$LiOH + LiHCO_3 \rightarrow H_2O + Li_2CO_3 \tag{3}$$

The Li_2CO_3 observed on the pristine sample results from the exposure to the air in the dry room. Li_2CO_3 is also found on the surface of the treated materials. However, $TMCO_3$ (i.e., $NiCO_3$ and $MnCO_3$) are more prevalent than Li_2CO_3, especially in the case of the LNMO-H_2O powder. Transition metal species have been identified as the main surface contaminant after long-term exposure to humidity in the extensive work on Ni-rich NMC by Gasteiger and coworkers.[31,38] The presence of predominantly $NiCO_3$ and $MnCO_3$ on the water-treated samples is further corroborated by the Mn_3S core level spectra,[39] where a decrease in the oxidation state of Mn is observed for the surface-treated samples (Figure S1, Supporting information). In the case of LNMO-H_2O, Mn has an oxidation state of +2, indicating that the Mn on the sample surface has almost completely reacted to form $MnCO_3$. Specifically, the main surface species are $TMCO_3$, alongside Li or TM hydroxides (pronounced peak at 532.2 eV in the O1s region). In contrast, a lower amount of $TMCO_3$ is found for LNMO-PA with regard to the C 1s spectra. This is also supported by the average oxidation state of Mn at the surface being +3 (Figure S1, Supporting Information), which may reflect a combination of Mn^{4+} (pristine LNMO crystal), Mn^{2+} (in the form of $MnCO_3$), and Mn^{+3} (for instance, in the form of $MnPO_4$).[40] In the bulk of the material, however, there is no change in oxidation state observed, neither for Mn nor for Ni, which is clearly present as Mn^{4+} and Ni^{2+} as evidenced by X-ray absorption spectroscopy (XAS) (Figure S2, Supporting Information). In contrast, the relatively lower amount of carbonates found on the surface of LNMO-PA is in accordance with the higher concentration of other surface species identified in the O 1s region, such as metal phosphates and, in particular, Li_3PO_4 (531 eV).[41] The predominant presence of Li_3PO_4 on the surface of LNMO-PA is further corroborated via

[31]P magic-angle spinning (MAS) nuclear magnetic resonance (NMR) spectroscopy (Figure 3c). The intense NMR peak at 13.1 ppm can be assigned to Li_3PO_4 with a shoulder at 6.2 ppm, while the less intense peak at 25.5 ppm might be the result of the presence of other phosphate species such as Li_2HPO_3 or LiH_2PO_4.[42]

To further support these assignments, thermogravimetric analysis (TGA) (**Figure 4**) coupled with mass spectrometry (MS) was performed to gain more information about the surface species and their thermal stability. In the temperature range between 30 and 600 °C, pristine LNMO shows a weight loss of 0.43%. In contrast, LNMO-H_2O and LNMO-PA lose 1.74% and 1.32%, respectively. The corresponding MS CO_2 signal ($m/z = 44$) shows a distinctive peak for LNMO-H_2O at around 400 °C. This coincides with the decomposition temperature of carbonates, for example, $MnCO_3$.[31] For LNMO-PA, however, only an extremely weak peak can be detected around 400 °C,

similarly to LNMO-REF. Therefore, the continuous mass loss of LNMO-PA, which starts from the beginning of the measurement, is mainly due to the release of remaining moisture and, potentially, phosphoric acid/hydrogen phosphates (between 200 and 400 °C).[43–45] This is in accordance with the results obtained by XPS and ^{31}P NMR, identifying Li_3PO_4 as the main surface species on LNMO-PA, while carbonates are mostly present on LNMO-H_2O.

2.2. Bulk Characterization

After having identified the surface composition of the materials, ^{7}Li MAS NMR (**Figure 5**a) was used to gain more insights into the bulk structure. The sharp peaks in the spectra of the four samples (a D_2O-treated sample was introduced to enhance the information depth for the subsequent ND measurements)
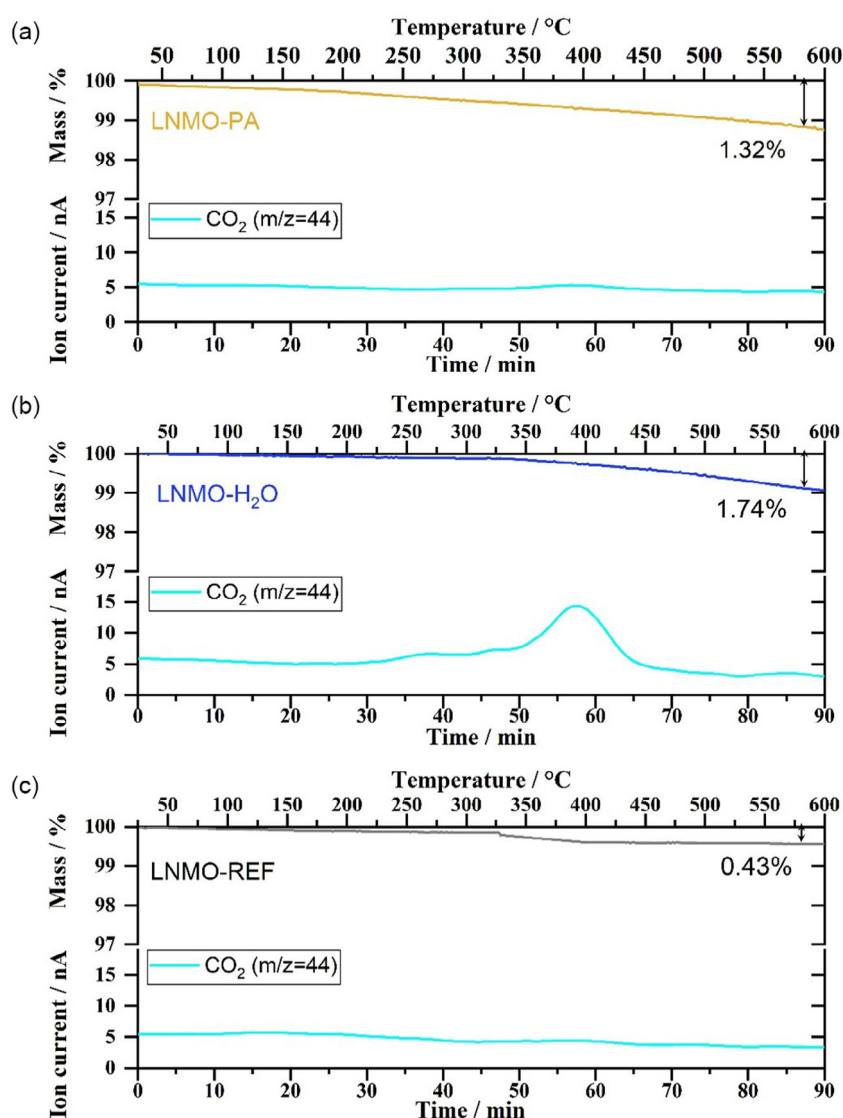

Figure 4. TGA-MS analysis under helium (20 mL min^{-1}) for a) LNMO-PA, b) LNMO-H_2O, and c) LNMO-REF. In the upper part of the three panels, the mass loss between 30 and 600 °C at a heating rate of 10 K min^{-1} is shown, and in the bottom the characteristic CO_2 signal ($m/z = 44$), as recorded by MS.
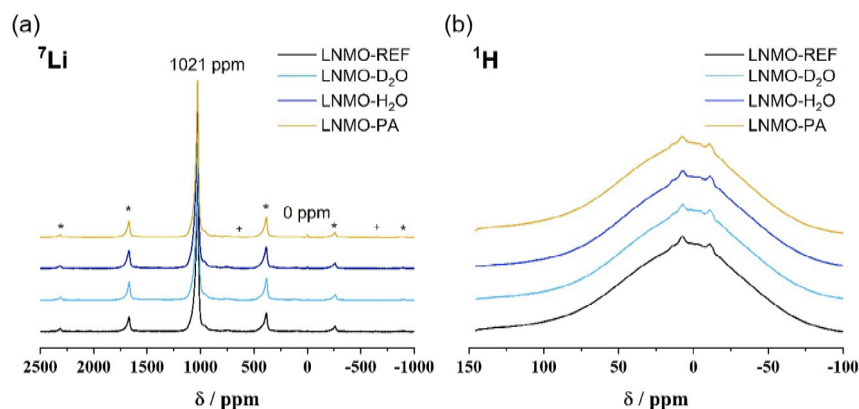
Figure 5. a) ^{7}Li and b) ^{1}H MAS NMR spectra of LNMO-REF, LNMO-H$_2$O, LNMO-D$_2$O, and LNMO–PA. The asterisks (*) in (a) mark the spinning sidebands of the peak at 1021 ppm, and the plus (+) marks the low-intensity peaks associated with the presence of layered Ni or Mn impurity phases such as Li$_2$MnO$_3$ or LiNi$_{0.5}$Mn$_{0.5}$O$_2$.

suggest that LNMO has an ordered spinel structure belonging to the $P4_332$ space group.[46] The very intense peak at 1021 ppm in Figure 5a can be assigned to Li$^+$ ions located at 8c sites, coordinated by 9 Mn^{4+} and 3 Ni^{2+} ions in 12d and 4b sites, respectively.[47] The peak shows a shoulder on each side for LNMO-H$_2$O (identical to LNMO-D$_2$O) and LNMO-PA. These shoulders might indicate a change in the coordination of the Li$^+$ ions in the 8c site, possibly resulting in a (partial) structural "disorder". In particular, the shoulders may derive from the local environments where the Li$^+$ ions are coordinated by only 8 Mn^{4+} but 4 Ni^{2+} (larger NMR shift) or 10 Mn^{4+} and 2 Ni^{2+} (smaller NMR shift), respectively.[46] Interestingly, for LNMO-H$_2$O and LNMO-D$_2$O, a very broad resonance band with low intensity can be seen at 750 ppm (indicated by a + in the spectrum). This band can be assigned to layered Ni or Mn impurity phases in the structure, such as Li$_2$MnO$_3$ or LiNi$_{0.5}$Mn$_{0.5}$O$_2$.[48] All samples show an additional resonance at 0 ppm. For LNMO-REF, LNMO-H$_2$O, and LNMO-D$_2$O, this band can be assigned to lithium impurities on the surface, for example, LiOH and Li$_2$CO$_3$.[49] For LNMO-PA, the band has a much higher intensity which is assigned to the high amount of Li$_3$PO$_4$ present on the particle surface, matching well the ^{31}P NMR results.

Considering all this information, it is concluded that Li$^+$ ions have been extracted from the structure to form the given surface species (Li$_3$PO$_4$ and various types of hydroxides and carbonates). However, it remains to be clarified whether these Li$^+$ ions come solely from the surface or even the bulk of the material. Especially for acidic treatments of Li-TM oxides, a pronounced Li$^+$/H$^+$ cation exchange has been reported.[50] Nonetheless, the ^{1}H MAS NMR spectra (Figure 5b) show only extremely weak resonances associated mainly with background contributions and do not reveal any significant differences between the four samples. These findings indicate that any possibly occurring Li$^+$/H$^+$ cation exchange appears to be limited to the very outer surface layers. In fact, this is in agreement with the essentially unaltered ^{7}Li NMR spectra discussed earlier herein and reported in the literature for layered lithium transition metal oxides, with the latter showing that such a cation exchange is only observed in the ^{2}H NMR spectra of materials treated with very aggressive

acids (e.g., 2.5 M sulfuric acid),[51] while a relatively mild acidic treatment comparable to the one described herein did not result in any changes of the NMR spectra.[51,52]

To investigate the eventual impact in more detail, in particular, any potential impact on the bulk structure, we carried out Raman spectroscopy, which is a powerful tool to differentiate between the two highly similar crystal structures of LNMO, that is, the disordered structure with the space group $Fd\bar{3}m$ and the ordered spinel structure with the space group $P4_332$.[53] The Raman spectra (Figure S3, Supporting information) confirmed the ordered $P4_332$ spinel structure, as already suggested by NMR and as indicated by the generally sharp peaks and distinct features in the 550–625 cm^{-1} region, resulting from ordered Ni and Mn.[54,55] The surface treatment had no visible effect on the Raman spectra of LNMO-H$_2$O and LNMO-PA, as no differences can be observed between the pristine and treated materials.

In the next step, synchrotron X-ray diffraction (sXRD) and ND experiments were performed. The combination of these two techniques is extremely powerful. In fact, sXRD has the advantage of being more sensitive to the heavier elements as the scattering takes place with the electron cloud and the interaction strength depends on the number of electrons with Z^2. In addition, sXRD offers a relatively high scattering angle resolution to easily separate overlapping peaks. Complementary to this, ND interacts with the nuclei and has no direct correlation of interaction strength with the periodic table which often leads to a better distinction of direct neighbor elements and isotopes of an element (e.g., hydrogen and deuterium).[56] Since ND has no angular dependent atomic form factor (scattering length) as compared to XRD, the scattered intensities at higher scattering angles are easier to detect. Additionally, the large illuminated sample volume and the high penetration depth of neutrons provide results with good statistics. In the combined Rietveld refinement, which was conducted to benefit from the complementary information provided by sXRD and ND, the patterns were refined simultaneously (**Figure 6**), further confirming the ordered spinel structure, with the lattice parameters being 8.1689(2) Å for LNMO-REF, 8.1695(2) Å for LNMO-H$_2$O and 8.1690(2) Å for LNMO-PA (**Table 1**).
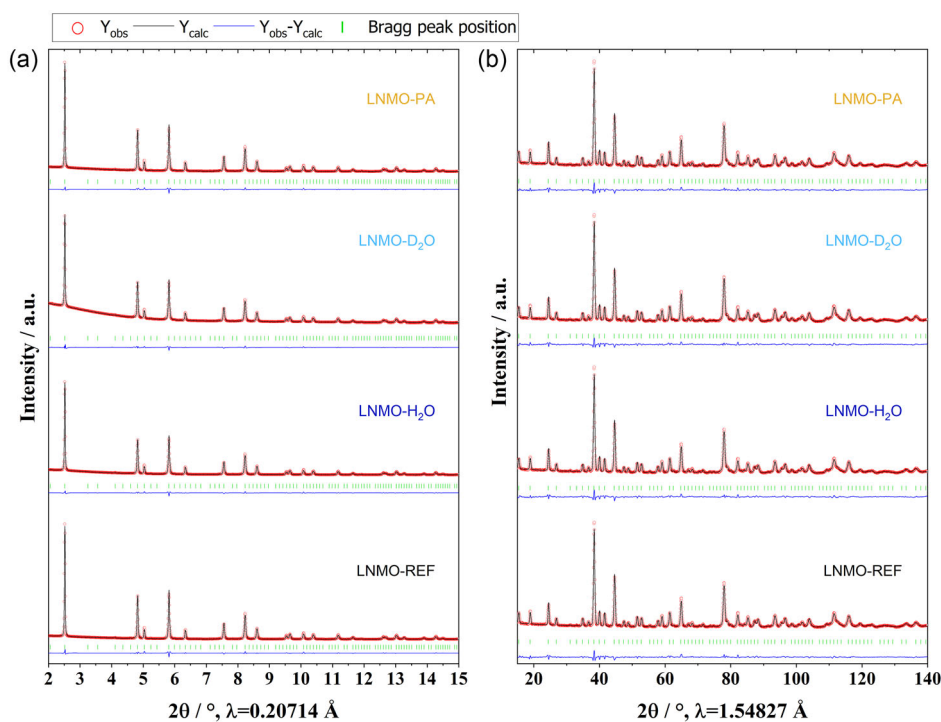
Figure 6. Combined Rietveld refinement of the a) synchrotron XRD data and b) neutron diffraction data of LNMO-REF, LNMO-H_2O, LNMO-D_2O, and LNMO-PA.

Table 1. Refinement parameters obtained from the ND data.

Sample	Space group	Lattice parameter from ND refinement [Å]	Cell volume from ND [Å³]	R_{wp} [%]	R_p [%]	R_{exp} [%]	χ2	Chemical formula from the combined refinement
LNMO-REF	$P4_332$	8.1689(2)	545.12(6)	4.31	3.16	2.32	1.86	$Li_{0.99}Ni_{0.48}Mn_{1.52}O_4$
LNMO-H_2O	$P4_332$	8.1695(2)	545.24(5)	3.85	2.85	2.43	1.59	$Li_{0.95}Ni_{0.48}Mn_{1.52}O_4$
LNMO-D_2O	$P4_332$	8.1699(2)	545.32(4)	3.73	2.73	2.53	1.47	$Li_{0.97}Ni_{0.49}Mn_{1.51}O_4$
LNMO-PA	$P4_332$	8.1690(3)	545.13(5)	4.07	2.98	2.41	1.69	$Li_{0.97}Ni_{0.49}Mn_{1.51}O_4$

In the XRD pattern, though, the superstructure peaks that are characteristic for the highly ordered $P4_332$ spinel structure are missing.[57] Therefore, a certain (partial) disorder between the Ni and Mn sites may be assumed, as it had also been indicated by the shoulders of the resonance band in the ^7Li NMR spectra. Following the refinement, the degree of such disorder is in the same range for all samples, with about 3% Ni ions in the 12d Mn sites and 10% Mn ions in the 4b Ni sites. This further corroborates the earlier findings, indicating that the surface treatment only affects the material surface, while the bulk material remains unchanged. For a more detailed investigation of a potential Li^+/H^+ exchange, we carefully compared LNMO-H_2O and LNMO-D_2O with the untreated reference and refined the diffraction data with a focus on H, D (or ^2H), and Li. In fact, H causes mainly incoherent scattering in the diffraction patterns equal to an increase in the background, while deuterated samples are characterized by a stronger coherent scattering from ^2H on the H

positions, leading to a much better refinement for the $Li^+/^2H^+$ cation exchange. From the refinement of the deuterated sample, a cation mixing of 3.6% can be determined (the refined parameters are listed in Table S1–S4, Supporting information), and it is reasonable to assume that it is in the same range as for LNMO-H_2O and presumably even a little higher for LNMO-PA with regard to the earlier discussed findings reported in the literature,[22,25–27] for which this value cannot be determined. Hence, the refinement of LNMO–D_2O shows that there is, indeed, a $Li^+/^{(2)}H^+$ cation exchange occurring during the aqueous (acidic) treatment. A $Li^+/^{(2)}H^+$ exchange of 3% was concluded for LNMO-PA, while for LNMO-H_2O and LNMO-D_2O, a $Li^+/^{(2)}H^+$ of 5% was determined. In fact, the chemical compositions calculated from the refined data agree well with those determined via inductively coupled plasma optical emission spectrometry (ICP-OES) (**Table 2**). In both cases, the pristine sample LNMO-REF has the highest Li content. Upon

Table 2. ICP data obtained for the solid (top) and liquid phase (bottom) after immersion of LNMO-REF (i.e., the pristine powder) in H_2O, D_2O, or PA.

		Li	Mn	Ni	Sum formula
Powders after treatment in	LNMO-REF	3.94%	46.28%	17.18%	$Li_{1.00}Ni_{0.52}Mn_{1.48}O_4$
	LNMO-H_2O	3.68%	45.93%	17.07%	$Li_{0.96}Ni_{0.53}Mn_{1.51}O_4$
	LNMO-D_2O	3.87%	46.18%	17.16%	$Li_{0.99}Ni_{0.52}Mn_{1.49}O_4$
	LNMO-PA	3.72%	45.49%	17.03%	$Li_{0.97}Ni_{0.53}Mn_{1.50}O_4$
Ions leached during treatment in	H_2O	4.42667 mg L^{-1}	0.05540 mg L^{-1}	0.01680 mg L^{-1}	–
	D_2O	5.73333 mg L^{-1}	0.06907 mg L^{-1}	0.02447 mg L^{-1}	–
	PA	3.70000 mg L^{-1}	3.67440 mg L^{-1}	1.27480 mg L^{-1}	–

$H_2O/D_2O/PA$ treatment, Li is removed from the structure, which leads to lower Li amounts for LNMO-H_2O, LNMO-D_2O, and LNMO-PA. Complementary ICP-OES measurements of the treatment solutions (H_2O, D_2O, and PA) after powder removal by centrifugation revealed that more lithium is leached into H_2O and D_2O than PA, which might be explained (at least to a large part) by the formation of Li_3PO_4 at the particle surface in the case of PA, which is "trapping" the lithium leached from

the LNMO structure and stabilizing the surface. Differently, the treatment solution of LNMO-H_2O (similarly to LNMO-D_2O) contained almost no transition metals, which might have been trapped as insoluble carbonates and hydroxides on the surface. The transition metal leaching was far more pronounced for LNMO-PA promoted through the acidic treatment, as reported for NMC cathode materials by Loeffler et al.[21]

2.3. Electrochemical Characterization

Finally, to correlate these findings with the electrochemical performance, electrodes were fabricated using conventional PVdF and NMP-based slurries to exclude any impact of the binder used. The long-term cycling data of the cells are shown in **Figure 7**a. During the initial cycles at 1C, LNMO-REF and LNMO-PA show a slightly reduced capacity compared to LNMO-H_2O, while the capacities are practically identical for the first cycles at C/3 (see **Table 3**). However, upon prolonged cycling, LNMO-H_2O shows significant capacity fading, resulting in a capacity retention of "only" 89% after 500 cycles. LNMO-PA provides a lower initial specific capacity, in fact, the lowest among the three materials tested, but much less capacity fading compared to both LNMO-H_2O and even LNMO-REF, achieving a capacity retention of 95% after 500 cycles compared to 93% for LNMO-REF; the latter still being significantly higher than for LNMO-H_2O. The specific capacities, capacity retentions, and Coulombic efficiencies averaged over a set of three cells during the long-term cycling are summarized in Table 3.

The first cycle dis-/charge profile (Figure 7b) of LNMO-PA shows an earlier onset of the slope around 4.75 V compared to LNMO-REF and LNMO-H_2O, which might be associated with an activation barrier on the active material surface and would also explain the reduced specific capacities at a slightly increased
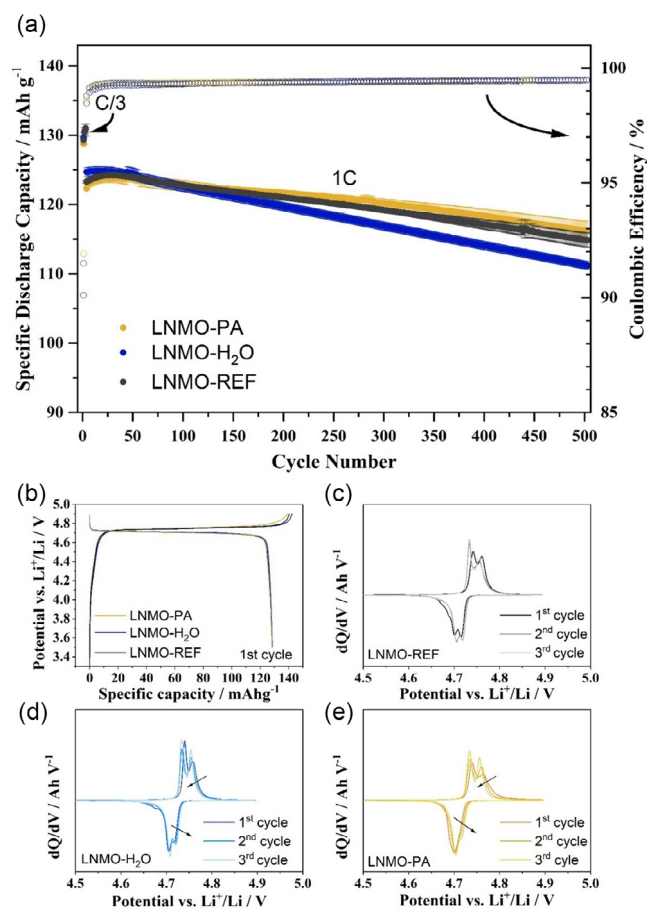

Figure 7. a) Evolution of specific discharge capacities of the differently treated LNMO powders upon prolonged cycling. The error bars indicate the standard deviation over at least triplicate cells. b) Potential profiles of the first cycle at C/3 and c–e) the corresponding differential capacity plots over the first three cycles.

Table 3. Characteristic performance parameters of the different Li|| LNMO cells.

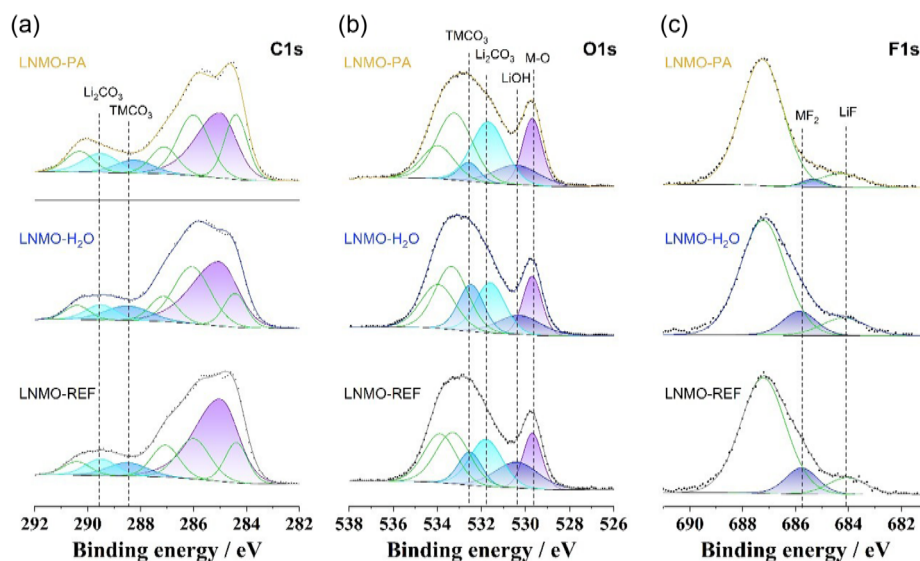|	ICE [%]	Average CE [%] (1C)	1st cycle C/3 discharge capacity [mAh g^{-1}]	1st cycle 1C discharge capacity [mAh g^{-1}]	500th cycle 1C discharge capacity [mAh g^{-1}]	Capacity retention at 1C [%]
LNMO-REF	91.5	99.3	129.3	123.3	114.8	93.1
LNMO-H_2O	90.1	99.4	129.6	124.7	111.2	89.2
LNMO-PA	91.9	99.4	128.8	122.3	116.2	95.0

Figure 8. Ex situ XPS spectra of the a) C 1s, b) O 1s, and c) F 1s photoelectron regions of the electrodes after 500 cycles.

C-rate. The differential capacity plots over the first three cycles (Figure 7c–e) reveal that this activation barrier in LNMO-PA can be observed in the form of a shift in the peak positions in the dQ/dV plot. Upon those initial 3 cycles, however, the activation barrier disappears while the peaks become sharper and more clearly separated for the $Ni^{2+/3+}$ and $Ni^{3+/4+}$ redox couples. Interestingly, a similar trend is observed for LNMO-H_2O, showing a peak shift in the dQ/dV plot during the first two to three cycles. A likely explanation for this behavior is the incremental release of H^+, which had occupied Li^+ sites in the structure during the initial cycles. The stronger polarization in the case of LNMO-PA, though, could also originate from the insulating metal phosphate layer that has formed on the LNMO surface and might hinder the electrode kinetics, as also reflected by the initially slightly lower capacity at 1C, while providing essentially the same capacity during the formation cycles at C/3, and slow down the re-exchange of Li^+ for H^+.

Nevertheless, the different surface species must also be responsible for the observed deviation in cycling stability and, thus, ex situ XPS measurements were conducted on electrodes recovered after 500 cycles (**Figure 8**). It is found that the amount of Li_2CO_3 (531.2 eV) increases for all samples compared to the noncycled powders (Figure 3a,b), which is due to carbonate-based electrolyte decomposition reactions.[58] Meanwhile, the amount of $TMCO_3$ stays comparably low and is still the lowest for LNMO-PA (see component at 532.2 eV in O1s spectra). In the F 1s region, LNMO-REF and LNMO-H_2O show, besides LiF (684.2 eV), a strong signal attributed to MF_2 (685 eV),[59] which is considerably weaker for LNMO-PA. Thus, the addition of PA leads to the stabilization of the cathode particles against the electrolyte through an artificial cathode electrolyte interphase (CEI), mostly composed of Li_3PO_4, which leads to the formation of less metal fluorides during cycling. In contrast, the presence of TM hydroxides and carbonates has a detrimental effect on the CEI stability, resulting in accelerated aging mechanisms, presumably through the release of CO_2 and other gaseous species during

cycling, as reported by Gasteiger and coworkers for Ni-rich NMC.[30,38,60–62] This explains the overall improved long-term cycling stability of LNMO-PA and the inferior performance of the material in contact with only water. With these results in mind, it can also be suggested that the accelerated capacity loss observed upon cycling of LNMO-H_2O (Figure 7) is related to the release of protons from the surface layer into the electrolyte, leading to faster degradation of the electrolyte and, therefore, diminishing the cycling stability.

3. Conclusion

The short-time exposure of $P4_332$-type $LiNi_{0.5}Mn_{1.5}O_4$ to (deuterated) water and phosphoric acid was investigated. Raman spectroscopy confirmed that the material possessed an ordered $P4_332$ structure, which did not change in the bulk upon exposure to water. This was also evidenced by sXRD and ND measurements. On the surface of the water-exposed materials, however, a thin amorphous layer could be identified via HRTEM. A detailed investigation of the surface using XPS suggests that LiOH is formed, which is later converted into carbonates, together with other surface species. The main surface species that were determined were $TMCO_3$ for LNMO-H_2O and predominantly Li_3PO_4 for LNMO-PA. Finally, the electrochemical performance of the treated materials was investigated on electrodes made using the conventional PVdF + NMP process to highlight the immediate impact of the aqueous treatments on the material itself. While the carbonates found on LNMO-H_2O clearly have a detrimental effect and result in the rapid capacity fading of the electrode (89% after 500 cycles), the opposite is true for the Li_3PO_4 found on LNMO-PA. This stabilizing surface layer has a positive impact on the performance leading to an improved capacity retention of 95% after 500 cycles, outperforming the untreated LNMO-REF with 93% capacity retention. Overall, this highlights that the exposure of LNMO to (acidic) water has no

**ADVANCED
SCIENCE NEWS**

www.advancedsciencenews.com

**ADVANCED
ENERGY & SUSTAINABILITY
RESEARCH**
Open Access

www.advenergysustres.com

detectable effect on the bulk structure but on the outermost particle surface—nonetheless, with a highly significant impact on the eventual performance of lithium battery cells.

4. Experimental Section

Materials Synthesis: LiNi$_{0.5}$Mn$_{1.5}$O$_4$ (LNMO) was synthesized by a continuous coprecipitation method followed by an optimized temperature treatment to tailor the particle size and morphology for high-voltage applications as reported earlier by Axmann et al.[63] For the surface treatment, the powder was mixed with deionized water (LNMO-H$_2$O), deuterated water (LNMO-D$_2$O), or diluted phosphoric acid (0.5 wt% in water; LNMO-PA) in a 1:2 powder to liquid ratio (i.e., 1 wt% phosphoric acid was added with respect to the active material powder). The surface treatment was carried out using a planetary ball mill (Fritsch Pulverisette) at 250 rpm for 2 h with a ball-to-powder weight ratio of 5:1, as described in an earlier study.[64] Afterward, the solutions were centrifuged to separate the powder from the liquid phase, and the powders were dried at 60 °C overnight.

Physicochemical Characterization: The elemental composition of the LNMO powders and the liquid phases was determined by ICP-OES, carried out using a Spectro Arcos spectrometer (Spectro Analytical Instruments). Scanning electron microscopy was performed utilizing a Zeiss Crossbeam XB340 field-emission electron microscope. Aberration corrected AC)-HRTEM was applied to compare the pristine LNMO with the surface-treated samples using an image C$_s$-corrected TEM FEI Titan 80–300 at 300 kV. XPS was performed using a Phoibos 150 XPS spectrometer with a monochromatic Al Kα ($h\nu$ = 1487 eV) X-ray source and a microchannel plate and Delay Line Detector (DLD). The scans were acquired with an X-ray source power of 400 W (15 kV), 30 eV pass energy, and 0.1 eV energy steps in a fixed analyzer transmission mode. The deconvolution of the spectra was carried out with the CasaXPS software, using a nonlinear Shirley-type background and 70% Gaussian and 30% Lorentzian profile functions.[65] A flood gun (i = 10 or 20 μA) was used to verify that the shift of the binding energy values was due to surface charging, caused by the insulating nature of the samples. All the samples were calibrated with respect to adventitious carbons at 285 eV.[32]

^{1}H, ^{7}Li, and ^{31}P MAS NMR spectroscopy was performed with a Bruker Avance neo spectrometer at a magnetic field of 4.7 T, corresponding to resonance frequencies of 200.2, 77.8, and 81.0 MHz, respectively. Spinning was performed in 1.3 mm rotors at a spinning speed of 50 kHz for ^{1}H/^{7}Li and 60 kHz for ^{31}P. Spectra were acquired with a single-pulse sequence for ^{1}H and a Hahn-echo sequence for ^{7}Li and ^{31}P. The pulse length was 3.0 μs for ^{1}H, 0.85 μs for ^{7}Li, and 0.95 μs for ^{31}P. The recycle delay was 10 s for ^{1}H and 1 s for ^{7}Li/^{31}P. Spectra were referenced to tetramethylsilane for ^{1}H, an aqueous 1M LiCl solution for ^{7}Li, and H$_3$PO$_4$ (85 wt%) for ^{31}P. The spectra intensities were normalized with respect to the sample mass and the number of scans.

Raman spectroscopy was carried out with an Alpha300 R (WiTec GmbH, Germany) confocal Raman microscope over a spectral range between −70 and 1108 rel. cm^{-1}. The system consists of a spectrometer with a grating of 1800 L mm^{-1} and a CCD-camera (1600 × 200 pixels) as well as a Nd:YAG laser with an excitation wavelength of 532 nm. The laser power was adjusted to 1.5 mW after microscope transit. The powders were measured using a 10× objective (Zeiss). sXRD was conducted at the P02.1 beamline of Petra III at DESY in Hamburg, Germany.[66] The X-rays had a wavelength of 0.20714 nm (≈60 keV). The samples were filled in boron silicate capillaries with a diameter of 0.5 mm and measured under constant rotation. The 2D data were collected using the Perkin Elmer XRD1621 CN3 - EHS (200 × 200 μm^2 pixel size, 2048 × 2048 pixel area) area detector and azimuthally integrated into the 1D data using the DAWN software.[67] The final 2θ range is from 2° to 15°. The LaB$_6$ powder (NIST 660c) standard was used to calibrate the measurement configuration. High-resolution neutron powder diffraction (ND) was performed at the SPODI instrument at the neutron source FRM II in Garching, Germany.[68] All measurements were performed in Debye–Scherrer

geometry with an incident neutron beam, having a rectangular cross-section at the sample position of 40 × 20 mm^2. Monochromatic neutrons with a wavelength of 1.54832(4) Å were chosen from the 551 reflection of a vertically focused composite germanium monochromator. High-resolution data were collected over a 2θ range from 1.0° to 151.9°. The samples were packed in vanadium cans that were sealed with indium wires. The containers were placed in a revolver-type sample changer where samples were measured under a constant rotation of a few hertz. For each sample, data were collected for about 3 h. The instrumental resolution function was determined from Na$_2$Ca$_3$Al$_2$F$_{14}$ powder serving as reference material and explicitly used for the calculation of the half-width of the reflections. Rietveld refinement was performed using Topas Academic. The neutron and XRD data were refined simultaneously. A Chebychev background was fitted, while the instrumental resolution was characterized using the Thompson–Cox–Hastings function. The cell parameters were determined from the neutron diffraction (ND) data. TGA was carried out using a Netzsch Libra 209 coupled with an Aeolos MS system. The measurements were carried out under a constant helium flow of 20 mL min^{-1} with a heating ramp of 10 K min^{-1}, following an isothermal step of 30 min at 30 °C. XAS was conducted at the XAFS beamline of the Elettra Synchrotron in Trieste, Italy. The storage ring was operated at 2.0 GeV with a ring current of 280 mA throughout the experiment. A fixed exit monochromator equipped with a pair of Si 111 single crystals was used to monochromatize the white beam. The samples were measured in the form of pellets in transmission mode and the three ionization chambers were filled with a mixture of nitrogen, helium, and argon to allow for good absorption before and after the sample as well as the reference. Manganese (6539 eV) and nickel (8333 eV) metal foils were used as reference and measured simultaneously with each scan to enable proper energy calibration of the resulting spectra. Normalization, background subtraction, energy calibration, and alignment of the spectra were performed with the Athena software of the Demeter package.[69] The absorption edge was determined as the first inflection point of the spectra in all cases.

Electrode Preparation: Electrodes were made with an active material to conductive carbon (Super C65, C-ENERGY, IMERYS) to binder (polyvinylidene difluoride, PVdF, Solef 6020, Solvay) ratio of 85:10:5. For the slurry preparation via planetary ball milling, a 4.0 wt% solution of PVdF in *N*-methyl-2-pyrrolidon (NMP; anhydrous, >99.5%; Sigma-Aldrich) was used. The resulting slurries were cast on battery-grade aluminum foil using a laboratory doctor blade equipment. After immediate pre-drying at 60 °C for 2 h, the resulting electrode tapes were stored at room temperature in the dry room overnight. Disk electrodes were punched and finally dried under vacuum for 14 h at 120 °C. The electrodes had an active material mass loading of 3.6–3.9 mg cm^{-2}.

Cell Assembly and Electrochemical Characterization: Three-electrode Swagelok cells with lithium-metal foils (thickness 500 μm, battery grade, Honjo) serving as counter and reference electrodes were used for the electrochemical characterization. The cell assembly was carried out in an argon-filled glove box (MB200B ECO, MBraun; H$_2$O and O$_2$ content <0.1 ppm) employing a glass fiber separator (Whatman GF/D) soaked with 240 μL of the electrolyte solution (1M LiPF$_6$ in ethylene carbonate (EC)/dimethyl carbonate (DMC), 1:1 w/w, UBE). Galvanostatic cycling was performed, setting the cut-off potentials to 3.5 and 4.9 V versus the Li$^+$/Li quasi-reference at 20 ± 2 °C, utilizing a Maccor Battery Tester 4300.

Supporting Information

Supporting Information is available from the Wiley Online Library or from the author.

Acknowledgements

Conflict of Interest

The authors declare no conflict of interest.

Data Availability Statement

The data that support the findings of this study are available from the corresponding author upon reasonable request.

Keywords

[1] D. Bresser, K. Hosoi, D. Howell, H. Li, H. Zeisel, K. Amine, S. Passerini, *J. Power Sources* **2018**, *382*, 176.

[2] M. Marinaro, D. Bresser, E. Beyer, P. Faguy, K. Hosoi, H. Li, J. Sakovica, K. Amine, M. Wohlfahrt-Mehrens, S. Passerini, *J. Power Sources* **2020**, *459*, 228073.

[3] M. Armand, P. Axmann, D. Bresser, M. Copley, K. Edström, C. Ekberg, D. Guyomard, B. Lestriez, P. Novák, M. Petranikova, W. Porcher, S. Trabesinger, M. Wohlfahrt-Mehrens, H. Zhang, *J. Power Sources* **2020**, *479*, 228708.

[4] J. U. Choi, N. Voronina, Y. K. Sun, S. T. Myung, *Adv. Energy Mater.* **2020**, *10*, 1.

[5] F. Nagler, N. Christian, A. Gronbach, F. Stahl, P. Daubinger, A. Flegler, M. Hofmann, G. A. Giffin, *ChemElectroChem* **2024**, *11*, e202300748.

[6] M. Heidbüchel, T. Schultz, T. Placke, M. Winter, N. Koch, R. Schmuch, A. Gomez-Martin, *ChemSusChem* **2023**, *16*, 1.

[7] G. Liang, V. K. Peterson, K. W. See, Z. Guo, W. K. Pang, *J. Mater. Chem. A* **2020**, *8*, 15373.

[8] B. Scrosati, J. Garche, *J. Power Sources* **2010**, *195*, 2419.

[9] M. M. Thackeray, J. R. Croy, E. Lee, A. Gutierrez, M. He, J. S. Park, B. T. Yonemoto, B. R. Long, J. D. Blauwkamp, C. S. Johnson, Y. Shin, W. I. F. David, *Sustainable Energy Fuels* **2018**, *2*, 1375.

[10] D. L. Wood, J. D. Quass, J. Li, S. Ahmed, D. Ventola, C. Daniel, *Dry. Technol.* **2018**, *36*, 234.

[11] D. Bresser, D. Buchholz, A. Moretti, A. Varzi, S. Passerini, *Energy Environ. Sci.* **2018**, *11*, 3096.

[12] A. C. Rolandi, I. de Meatza, N. Casado, M. Forsyth, D. Mecerreyes, C. Pozo-Gonzalo, *RSC Sustain.* **2024**, *2*, 2125.

[13] R. Sahore, D. L. Wood, A. Kukay, K. M. Grady, J. Li, I. Belharouak, *ACS Sustainable Chem. Eng.* **2020**, *8*, 3162.

[14] B. Starke, S. Seidlmayer, O. Dolotko, R. Gilles, K. H. Pettinger, *Energies* **2017**, *10*, 1.

[15] B. Starke, S. Seidlmayer, S. Jankowsky, O. Dolotko, R. Gilles, K. H. Pettinger, *Sustainability* **2017**, *9*, 888.

[16] J. C. Knight, S. Therese, A. Manthiram, *J. Electrochem. Soc.* **2015**, *162*, A426.

[17] W. B. Hawley, A. Parejiya, Y. Bai, H. M. Meyer, D. L. Wood, J. Li, *J. Power Sources* **2020**, *466*, 228315.

[18] J. He, G. Melinte, M. S. D. Darma, W. Hua, C. Das, A. Schökel, M. Etter, A. Hansen, L. Mereacre, U. Geckle, T. Bergfeldt, Z. Sun, M. Knapp, H. Ehrenberg, J. Maibach, *Adv. Funct. Mater.* **2022**, *32*, 2207937.

[19] A. I. Pitillas, L. L. De Taeye, P. M. Vereecken, *Adv. Mater. Interfaces* **2024**, *11*, 1.

[20] L. Hartmann, D. Pritzl, H. Beyer, H. A. Gasteiger, *J. Electrochem. Soc.* **2021**, *168*, 070507.

[21] N. Loeffler, G. T. Kim, F. Mueller, T. Diemant, J. K. Kim, R. J. Behm, S. Passerini, *ChemSusChem* **2016**, *9*, 1112.

[22] M. Kuenzel, D. Bresser, T. Diemant, D. V. Carvalho, G. T. Kim, R. J. Behm, S. Passerini, *ChemSusChem* **2018**, *11*, 562.

[23] I. Doberdò, N. Löffler, N. Laszczynski, D. Cericola, N. Penazzi, S. Bodoardo, G. T. Kim, S. Passerini, *J. Power Sources* **2014**, *248*, 1000.

[24] G. T. Kim, N. Löffler, I. Doberdo, N. Laszczynski, D. Bresser, S. Passerini, *Method for Producing an Electrode for a Lithium-Ion Battery* **2015**.

[25] S. Sananes-Israel, I. Urdampilleta, G. Kvasha, I. Landa-Medrano, I. de Meatza, *Batter. Supercaps* **2024**, *7*, 202400358.

[26] P. Zhu, V. Trouillet, S. Heißler, W. Pfleging, *J. Energy Storage* **2023**, *66*, 107401.

[27] H. Chen, A. M. Mattsson, L. King, H. Liu, I. Nielsen, T. Ericson, A. Preobrajenski, W. R. Brant, M. Hahlin, *J. Mater. Chem. A* **2024**, *12*, 25393.

[28] A. R. Schuer, M. Kuenzel, S. Yang, M. Kosfeld, F. Mueller, S. Passerini, D. Bresser, *J. Power Sources* **2022**, *525*, 231111.

[29] S. E. Renfrew, B. D. McCloskey, *J. Am. Chem. Soc.* **2017**, *139*, 17853.

[30] D. Pritzl, T. Teufl, A. T. S. Freiberg, B. Strehle, J. Sicklinger, H. Sommer, P. Hartmann, H. A. Gasteiger, *J. Electrochem. Soc.* **2019**, *166*, A4056.

[31] J. Sicklinger, M. Metzger, H. Beyer, D. Pritzl, H. A. Gasteiger, *J. Electrochem. Soc.* **2019**, *166*, A2322.

[32] C. D. Wagner, W. M. Riggs, L. E. Davis, J. F. Moulder, *Handbook of X-Ray Photoelectron Spectroscopy: A Reference Book of Standard Use in X-Ray Photoelectron Spectroscopy*, Perkin-Elmer Corporation. Physical Electronics Division, Eden Prairie, Minnesota **1979**.

[33] A. Etxebarria, S. L. Koch, O. Bondarchuk, S. Passerini, G. Teobaldi, M. Á. Muñoz-Márquez, *Adv. Energy Mater.* **2020**, *10*, 202000520.

[34] K. N. Wood, G. Teeter, *ACS Appl. Energy Mater.* **2018**, *1*, 4493.

[35] M. Zarrabeitia, M. Casas-Cabanas, M. Á. Muñoz-Márquez, *Electrochim. Acta* **2021**, *372*, 137846.

[36] Z. Chen, H. D. Nguyen, M. Zarrabeitia, H. P. Liang, D. Geiger, J. K. Kim, U. Kaiser, S. Passerini, C. Iojoiu, D. Bresser, *Adv. Funct. Mater.* **2021**, *31*, 1.

[37] I. A. Shkrob, J. A. Gilbert, P. J. Phillips, R. Klie, R. T. Haasch, J. Bareño, D. P. Abraham, *J. Electrochem. Soc.* **2017**, *164*, A1489.

[38] R. Jung, R. Morasch, P. Karayaylali, K. Phillips, F. Maglia, C. Stinner, Y. Shao-Horn, H. A. Gasteiger, *J. Electrochem. Soc.* **2018**, *165*, A132.

[39] M. Kuenzel, G.-T. T. Kim, M. Zarrabeitia, S. D. Lin, A. R. Schuer, D. Geiger, U. Kaiser, D. Bresser, S. Passerini, *Mater. Today* **2020**, *39*, 127.

[40] V. R. Galakhov, M. Demeter, S. Bartkowski, M. Neumann, N. A. Ovechkina, E. Z. Kurmaev, N. I. Lobachevskaya, Y. M. Mukovskii, J. Mitchell, D. L. Ederer, *Phys. Rev. B - Condens. Matter Mater. Phys.* **2002**, *65*, 1.

[41] B. V. R. Chowdari, K. L. Tan, W. T. Chia, *Solid State Ionics* **1992**, *53–56*, 1172.

[42] I. L. Mudrakovskii, V. P. Shmachkova, N. S. Kotsarenko, V. M. Mastikhin, *J. Phys. Chem. Solids* **1986**, *47*, 335.

[43] S. G. Shankwalkar, C. Cruz, *Ind. Eng. Chem. Res.* **1994**, *33*, 740.

[44] J. Xiao, W. Xu, D. Choi, J.-G. Zhang, *J. Electrochem. Soc.* **2010**, *157*, A142.

[45] H. S. Barud, C. A. Ribeiro, M. S. Crespi, M. A. U. Martines, J. Dexpert-Ghys, R. F. C. Marques, Y. Messaddeq, S. J. L. Ribeiro, *J. Therm. Anal. Calorim.* **2007**, *87*, 815.

[46] J. Cabana, M. Casas-Cabanas, F. O. Omenya, N. A. Chernova, D. Zeng, M. S. Whittingham, C. P. Grey, *Chem. Mater.* **2012**, *24*, 2952.

[47] H. Duncan, B. Hai, M. Leskes, C. P. Grey, G. Chen, *Chem. Mater.* **2014**, *26*, 5374.

[48] J. Bréger, Y. S. Meng, Y. Hinuma, S. Kumar, K. Kang, Y. Shao-Horn, G. Ceder, C. P. Grey, *Chem. Mater.* **2006**, *18*, 4768.

[49] C. P. Grey, N. Dupré, *Chem. Rev.* **2004**, *104*, 4493.

[50] I. Hamam, N. Zhang, A. Liu, M. B. Johnson, J. R. Dahn, *J. Electrochem. Soc.* **2020**, *167*, 130521.

[51] Y. Paik, C. P. Grey, C. S. Johnson, J. S. Kim, M. M. Thackeray, *Chem. Mater.* **2002**, *14*, 5109.

[52] F. Dogan, J. R. Croy, M. Balasubramanian, M. D. Slater, H. Iddir, C. S. Johnson, J. T. Vaughey, B. Key, *J. Electrochem. Soc.* **2015**, *162*, A235.

[53] B. Aktekin, F. Massel, M. Ahmadi, M. Valvo, M. Hahlin, W. Zipprich, F. Marzano, L. Duda, R. Younesi, K. Edström, D. Brandell, *ACS Appl. Energy Mater.* **2020**, *3*, 6001.

[54] B. Aktekin, M. Valvo, R. I. Smith, M. H. Sørby, F. Lodi Marzano, W. Zipprich, D. Brandell, K. Edström, W. R. Brant, *ACS Appl. Energy Mater.* **2019**, *2*, 3323.

[55] P. Stüble, S. Indris, M. Müller, H. Gesswein, J. R. Binder, *J. Mater. Chem. A* **2022**, *10*, 9010.

[56] R. Gilles, *J. Surf. Investig.* **2020**, *14*, S69.

[57] G. Gabrielli, P. Axmann, M. Wohlfahrt-Mehrens, *J. Electrochem. Soc.* **2016**, *163*, A470.

[58] B. L. D. Rinkel, D. S. Hall, I. Temprano, C. P. Grey, *J. Am. Chem. Soc.* **2020**, *142*, 15058.

[59] J. F. Moulder, W. F. Stickle, P. E. Sobol, K. D. Bomben, *Handbook of X-Ray Photoelectron Spectroscopy*, Physical Electronics Inc., Minnesota (US) **1992**.

[60] S. Jeong, J. Kim, J. Mun, *J. Electrochem. Soc.* **2019**, *166*, A5038.

[61] S. S. Zhang, *Front. Energy Res.* **2014**, *2*, 2.

[62] A. T. S. Freiberg, J. Sicklinger, S. Solchenbach, H. A. Gasteiger, *Electrochim. Acta* **2020**, *346*, 136271.

[63] P. Axmann, G. Gabrielli, M. Wohlfahrt-Mehrens, *J. Power Sources* **2016**, *301*, 151.

[64] M. Kuenzel, H. Choi, F. Wu, A. Kazzazi, P. Axmann, M. Wohlfahrt-Mehrens, D. Bresser, S. Passerini, *ChemSusChem* **2020**, *13*, 2650.

[65] J. Walton, P. Wincott, N. Fairley, A. Carrick, *Peak Fitting with CasaXPS: A Casa Pocket Book*, Accolyte Science, Knutsford, UK **2010**.

[66] A. C. Dippel, H. P. Liermann, J. T. Delitz, P. Walter, H. Schulte-Schrepping, O. H. Seeck, H. Franz, *J. Synchrotron Radiat.* **2015**, *22*, 675.

[67] J. Filik, A. W. Ashton, P. C. Y. Chang, P. A. Chater, S. J. Day, M. Drakopoulos, M. W. Gerring, M. L. Hart, O. V. Magdysyuk, S. Michalik, A. Smith, C. C. Tang, N. J. Terrill, M. T. Wharmby, H. Wilhelm, *J. Appl. Crystallogr.* **2017**, *50*, 959.

[68] M. Hoelzel, A. Senyshyn, N. Juenke, H. Boysen, W. Schmahl, H. Fuess, *Nucl. Instruments Methods Phys. Res. Sect. A: Accel. Spectrometers, Detect. Assoc. Equip.* **2012**, *667*, 32.

[69] B. Ravel, M. Newville, *J. Synchrotron Radiat.* **2005**, *12*, 537.